ADVANCED MATERIALS
www.advmat.de

Shape-Evolving Structured Liquids

*Paul Y. Kim, Shipei Zhu, Joe Forth, Ganhua Xie, David A. King, Brett A. Helms, Paul D. Ashby, Ahmad K. Omar, and Thomas P. Russell**

Migration, division, and reconfiguration – functions essential to living systems – are driven by active processes. Developing synthetic mimics is an outstanding challenge. Lipid bilayers that bound natural systems are locally deformed by active species, e.g., microtubules, but the resulting non-equilibrium shapes relax when active species motion ceases, and the shape changes lack immediate control. A fully synthetic system is described, driven by active particles encapsulated by a reconfigurable nanoparticle-surfactant membrane that undergoes shape fluctuations reminiscent of living cells. These shape changes are preserved after particle activity stops. Surfactant concentration tunes the interfacial tension over three orders of magnitude, making on-demand shape evolution possible. Directional migration, division, and reconfiguration across multiple scales are possible, leading to a new class of biomimetic, reconfigurable, and responsive materials, paving the way for autonomous synthetic machines.

1. Introduction

Active matter plays a crucial role in shaping cells and bacteria, enabling essential biological functions, like motility, division, reconfiguration, and replication. Intracellular actin networks generate leading-edge protrusions, e.g., lamellipodia and filopodia, by impinging onto and locally deforming the lipid-bilayer cell membrane, enabling directional cell migration.[1–4] To design artificial systems capable of dynamic, life-like functions, both synthetic and natural complex systems that actively consume energy have been investigated.[5,6] Given the ease with which they can be produced and have their composition altered, droplets make for particularly promising platforms for producing synthetic, soft, active systems.[7,8] However, while droplet-based Marangoni swimmers are comparatively easy to formulate,[9] the design rules by which one might make systems of droplets capable of deforming themselves are still unclear, often requiring the incorporation of complex biological parts.[10] Natural microtubule filaments, fueled by ATP hydrolysis, exhibit chaotic flow at aqueous two-phase droplet interfaces, driving spontaneous droplet motility.[11] Chaotic flow of active microtubule networks can also shape the water-water interface with ultralow interfacial tension and control the dynamics of aqueous phase separation, such as disrupting interface continuity and driving droplet generation.[12,13] However, this active force is insufficient to deform liquid interfaces, such as water-oil interfaces and liquid-air surfaces, with high interfacial tension. In contrast, active particles, such as self-propelled active nematics[14,15] and active colloids powered by electric/magnetic fields,[16–18] can generate stronger active force by internal active flow or particle-interface collisions to induce dramatic shape changes of membraneless liquid-in-air droplets. Self-propelled particles encapsulated in giant unilamellar vesicles locally deform the lipid membranes, resulting in dramatic shape changes, including

P. Y. Kim, S. Zhu, D. A. King, B. A. Helms, P. D. Ashby, A. K. Omar, T. P. Russell
Materials Sciences Division
Lawrence Berkeley National Laboratory
Berkeley, CA 94720, USA
E-mail: russell@mail.pse.umass.edu

J. Forth
Department of Physics
University of Liverpool
Liverpool L69 7ZE, UK

J. Forth
Department of Chemistry
University of Liverpool
Liverpool L69 7ZD, UK

G. Xie
State Key Laboratory of Chemo and Biosensing
College of Chemistry and Chemical Engineering
Hunan University
Changsha 410082, China

D. A. King, A. K. Omar
Department of Materials Science and Engineering
University of California
Berkeley, CA 94720, USA

B. A. Helms, P. D. Ashby
The Molecular Foundry
Lawrence Berkeley National Laboratory
Berkeley, CA 94720, USA

T. P. Russell
Polymer Science and Engineering Department
University of Massachusetts
Amherst, MA 01003, USA

T. P. Russell
Advanced Institute for Materials Research (AIMR)
Tohoku University
Sendai 980-8577, Japan

The ORCID identification number(s) for the author(s) of this article can be found under https://doi.org/10.1002/adma.202500804

DOI: 10.1002/adma.202500804

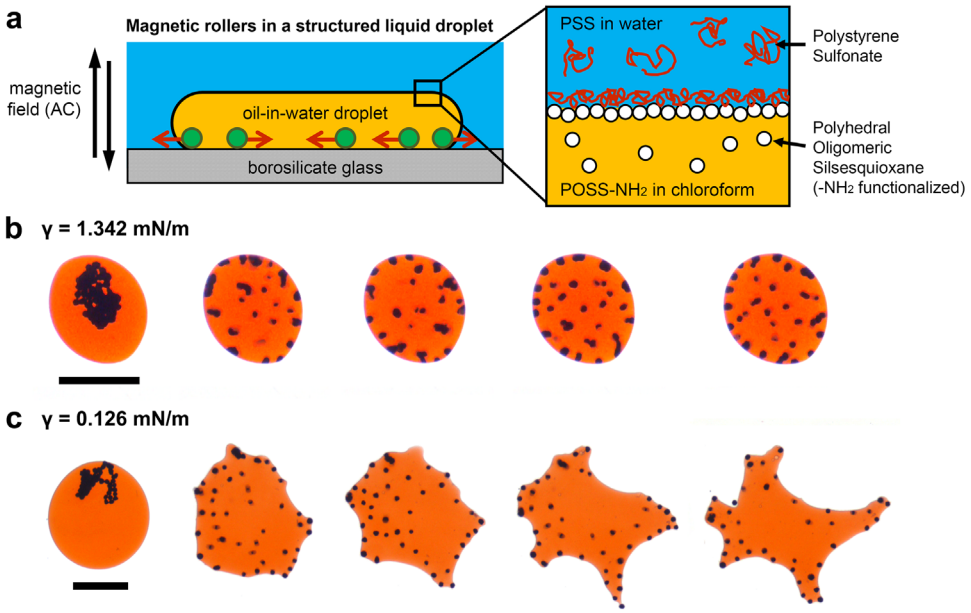

Figure 1. Shape evolving structured liquid driven by active magnetic rollers a) Schematics of the experiment and a magnified scheme of the oil—water interface. b) Time-lapse images of the deformation of typical structured liquid droplets with an interfacial tension of 1.342 mN $m^{-1}$and c) 0.126 mN m^{-1}. 80 μm nickel particles (black dots) turn into active rollers under a vertical magnetic AC field of 3.5 mT, 30 Hz square wave. The images in 1c were taken from Video S1 (Supporting Information) where the times provided are when the magnetic field was turned on. The images in 1b are over the same time period. The scale bar sizes are 1 mm.

tether-like protrusions and highly branched structures.[19–21] But the shape changes in these systems are not permanent, as the bare liquid–liquid or liquid-air interface and the lipid membrane will relax elastically when motion of the active matter ceases. The properties of the biological materials used in these complex systems are also intrinsically predetermined, limiting their tunability.

Structured liquids, produced by the interfacial formation, assembly, and jamming of nanoparticle surfactants (NPSs), are reconfigurable and, due to the tunability of the interfacial tension, γ, over three orders of magnitude (from $\approx 10^{1}$ down to $\approx 10^{-2}$ mN m^{-1}), provide an ideal platform for generating evolutionary, energy-interconverting systems.[22] Here, we show that, when subjected to an AC magnetic field, paramagnetic spherical particles roll and aggregate at the interface of an oil droplet at which NPSs are assembled, resulting in directional shape changes, as well as division and translational motion of the droplet. The active particles continuously push on and locally deform the membrane which is tuned to have a sufficiently low interfacial tension by the NPS assembly. This deformation generates additional bare interfacial area, resulting in more NPSs binding to newly exposed interfacial area. Relaxing back to the pre-deformed state would thus require the ejection of these newly bound NPSs, a process with stiff kinetic limitations. As a result, these jammed NPS assemblies can lock in these deformations for extraordinarily long timescales. Active particles accumulate at locally deformed convex surfaces, further amplifying the irreversible deformation, generating a protrusion or tether that is preserved when the activity-inducing field is removed and the active particle motion ceases. The kinetics of structural evolution depends on the activity of the particles, the interfacial tension of the NPS membrane, droplet size, and the contact angle of the encapsulated liquid with the substrate. The NPS assemblies in the evolutionary systems described here are more tunable than classic amphiphile bilayers and establish a platform to replicate natural systems and to design artificial autonomous machines from the microscopic to the macroscopic length scales.

2. Results and Discussion

A chloroform droplet containing nickel particles (≈40 particles in 1.5 μL) with diameters of 80±19 μm is deposited in a pool of water on a leveled, oxygen-plasma cleaned, borosilicate cover glass, as illustrated in **Figure** 1a. The density contrast between chloroform and water results in the droplet resting on the glass. The hydrophilic surface of the substrate increases the contact angle of the droplet (from 90.8° to 146°), preventing the encapsulated active particles from being trapped at the edge of the droplet. Negatively charged polystyrene sulfonate (PSS), a surfactant, with M_w = 7,000 g mol^{-1} is dissolved in the water, while positively charged POSS-NH_3Cl nanoparticles with diameters of 1.5 nm are dispersed in the chloroform. The opposing electrostatic charge of these two components results in their assembly into NPSs at the oil—water interface and a reduction in the oil—water interfacial tension, γ. By varying the concentration of both PSS and POSS-NH_3Cl between 0 and 80 mg mL^{-1}, we can continuously vary γ from 22 down to 37 μN m^{-1} (Table S1, Supporting Information). For droplets with high surface tensions (γ = 1.342 mN m^{-1}, Figure 1b), the incorporated ferromagnetic active Ni rollers,[23] which are energized by an AC magnetic field of 3.5 mT and a 30 Hz square wave applied normal to the substrate surface (Figure 1a), disperse within the droplets and accumulate at their edges, but cause no perceptible shape changes to the droplets. A typical example of this behavior is shown in

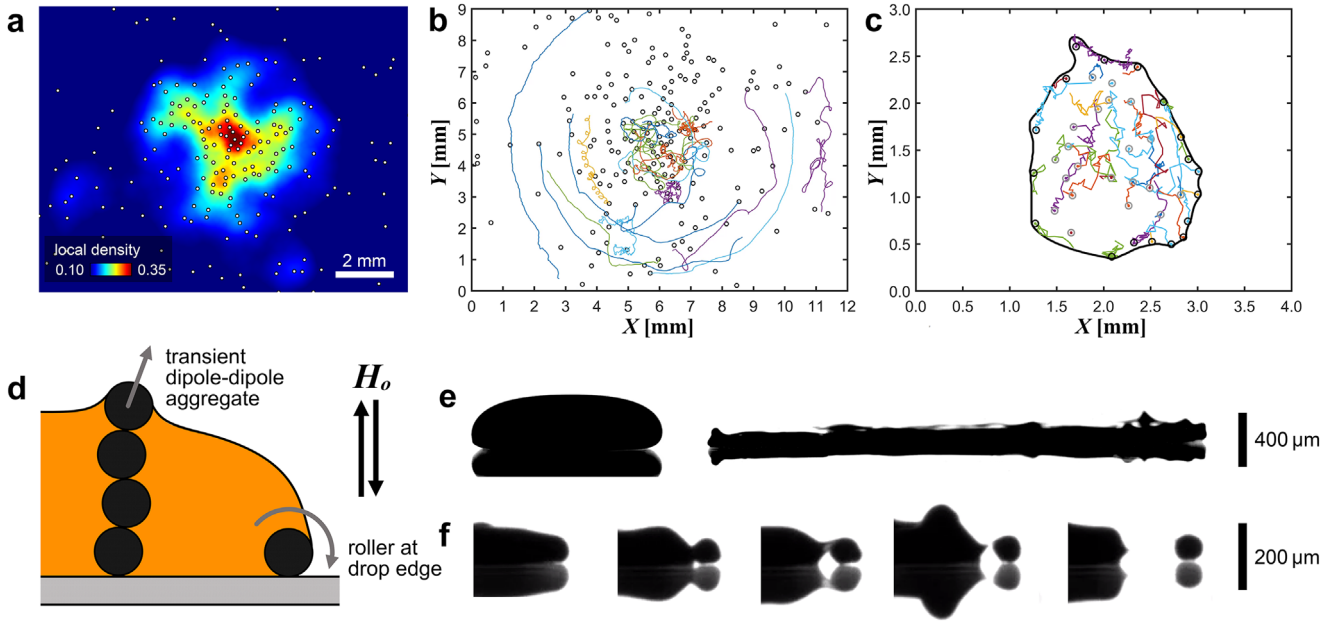

Figure 2. Membrane deformations by active magnetic rollers. Local number densities a) and trajectories b) of randomly selected particles in an unbounded fluid. c) Trajectories of confined particles in a droplet at an early stage (≈4s). d) Schematics of the side-view of interfacial deformation by magnetic rollers. e) Droplet before (left) and after (right) deformation by rollers from side view. f) Time-lapse side view images with a ≈2s interval of magnetic rollers deforming a droplet and generating a satellite droplet.

Figure 1b. As droplet surface tensions are reduced to 0.126 mN m^{-1} (Figure 1c), the response of their interfaces to the active particles changes significantly. Under such low interfacial tension conditions, the interfacial membrane deforms, the deformation is amplified, and a protrusion grows from the circular droplet as the particles perform work on the NPS membrane encapsulating the droplet (see Figure 1c and Movie S1, Supporting Information for typical examples). The active particle size also plays an important role as demonstrated in Figure S1 (Supporting Information), with the extent of droplet deformation increasing enormously as the active particle diameter is increased from 40 μm up to 140 μm. Driven entirely by the external field, the system does not exhibit unwanted effects, such as fuel depletion and flow disturbances, observed in swimmers propelled by chemical reactions.

In an unbounded fluid without a surrounding aqueous phase, the active particles gathered within a 1.8 mm radius from the center, where the magnetic field is relatively uniform (**Figure 2a**). When a 30 Hz square-wave, 3.5 mT magnetic field was applied to the system, the instantaneous speed of these unbounded active particles ranged from 1 to 5 mm s^{-1} and appeared independent of local particle density (Figure S2a–c, Supporting Information), however the persistence length of the particles trajectories decreased in denser areas due to the increased particle-particle interactions (including magnetic dipole–dipole interactions) (Movie S2, Supporting Information). The pair correlation function of the particle locations indicated that particles maintained a minimum center-to-center separation of 2.9d (d is particle diameter ≈80 μm, Figure S2d, Supporting Information) from each other, a result of the combined magnetic repulsive and hydrodynamic forces.[24,25] The particle speed showed a strong dependence on the frequency of the applied magnetic field, with both the speed and width of the speed distribution increasing as frequency was increased from 10 to 60 Hz (Figure S3a–d, Supporting Information). Similarly, the persistence length of the particles varied strongly with the oscillation frequency of the magnetic field, ranging from ≈1.7 mm at 10 Hz down to ≈0.1 mm at 60 Hz (Figure S3e, Supporting Information). A frequency of 30 Hz is used in these studies, where the particles show a more uniform speed distribution (Figure S3a, Supporting Information) and the persistence length of the particle trajectories is comparable to the typical droplet diameter, ≈0.5–1 mm. The encapsulated active particles are thus significantly confined. In some instances, the aspherical shape of the ferromagnetic particles led to a rocking motion at low-frequency fields and a rolling motion with a chirality in the 2D projected helical trajectories at frequencies above 10 Hz, consistent with observations made in a previous study.[23] Finally, we note that motion in this system is dominated by viscous dissipation, and the rolling motions stop when the field is removed.

Upon confinement within a droplet, the persistent motion of the particles resulted in their migration to the edges of the droplet over time (Figure 2c). Side view images show strong vertical deformations of the droplet by the particles and elucidate the mechanism of droplet deformation (Figure 2d–f). As evidenced in Figure 2f, the membrane deformation is driven primarily by particles that are obstructed by the droplet membrane but energized to keep rolling. This figure also confirms that the deformed shape is preserved by NPS membrane. Transient stacks of particles, which form vertically along the magnetic field in denser areas, exceed the height of the droplet near the droplet–substrate contact line, leading to large vertical deformations of the droplet (Movie S3, Supporting Information), while the outward push from the rolling particles deforms the membrane horizontally. These

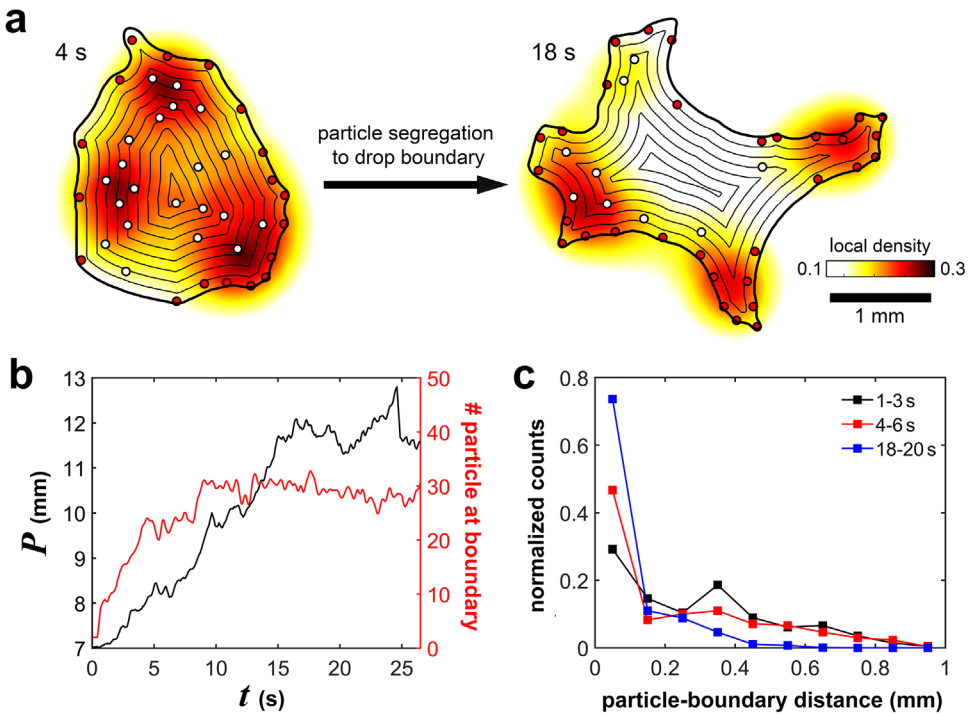

Figure 3. Particle segregation to the droplet membrane due to persistent motions of particles. a) Distribution of particles in the droplet, 4 and 18 s after switching the magnetic field on. Contour lines are separated by 0.1 mm. The number of particles at the drop boundary (red) becomes larger than that in the bulk phase (white). b) Droplet perimeter and the number of particles at the boundary as a function of time. c) Normalized number of particles as a function of particle-to-boundary distance at different times.

deformed membrane shapes are then locked in-place by the assembly and jamming of NPS.

The confined active magnetic particles rapidly accumulate at the droplet membrane wall[26–29] as shown in **Figure** 3a. In an initial growth phase, the length of the perimeter of a 2D projection of the droplet shape increased linearly with time due to membrane deformation, revealing the constant growth rate of the protrusion edges (Figure 3b) before eventually plateauing. This plateau is reached 15 s after the initial deformation began and is determined by the conservation of droplet volume. The droplet height (as measured from the substrate) was not observed to decrease below ≈130 µm (Figure 2e). The droplet center was depleted of particles within 10 s after the external field was applied, and more particles migrated to the droplet membrane wall as the perimeter of the droplet increased. Figure 3c shows the distribution of particle-to-membrane distances at different stages of perimeter growth, indicating that the fraction of particles in contact with the membrane progressively increases up to 80% until the perimeter reaches the plateau. A fraction of particles remained separated from the membrane wall despite the increasing perimeter, which is attributed to magnetic repulsions by particles at the membrane, a preference for accumulation at locations where the membrane wall is more outwardly deformed from the droplet, as shown in Figure 3a, and, since the particles continue to spin, some fraction of particles will eventually spin away from the wall.

The magnitude of active force, F^{act}, can be equated to the drag force by assuming that interparticle interactions are negligible under the dilute condition. In the absence of particle interactions, the drag force is estimated as $3\pi\eta d v^{act}$ for unbounded spheres in three dimensions, where η is the solvent (chloroform) viscosity, and $v^{act}$is the active particle velocity. The strength of the active forces relative to the interfacial forces determines whether the active particles can drive significant membrane deformations. To quantify this, let us consider the active force required to produce a protuberance of size R, which we shall treat as approximately circular for simplicity. As such, the active particles must overcome the Laplace pressure, $P_\gamma = \gamma / R$ imposed by the surface tension. Here, we have neglected any changes in the height of the droplets, which are much smaller than their in-plane deformations. Ignoring negligible hydrodynamic effects, the active particles can only apply a force on the membrane while in contact with it. If a number, N, of active particles are at the membrane wall, they will exert a total force, NF^{act}, over an area $d\,L$, where L is the perimeter of the membrane. Comparing the "active pressure", $P_{act} = NF^{act}/d\,L$, to the Laplace pressure and using our measured tensions we estimate that $N/L \approx 4.8\ \mathrm{mm}^{-1}$ active particles per-unit-length of membrane perimeter are sufficient to produce a deformation of order $R = 1$ mm.

This estimation compares favorably with experimental observations. In Figure 3a, we see protrusions whose perimeter is ≈ 2 mm sustained by eight or nine particles. Similarly, **Figure** 4b shows that deformations begin to present themselves after 7s when, from Figure 3b, the average line density of active particles at the membrane is approaching 4 mm^{-1}. A corollary of our estimate is that those parts of the droplet perimeter where the active particles have most densely accumulated shall be most noticeably affected. This is demonstrated in Figure 3a, where the three

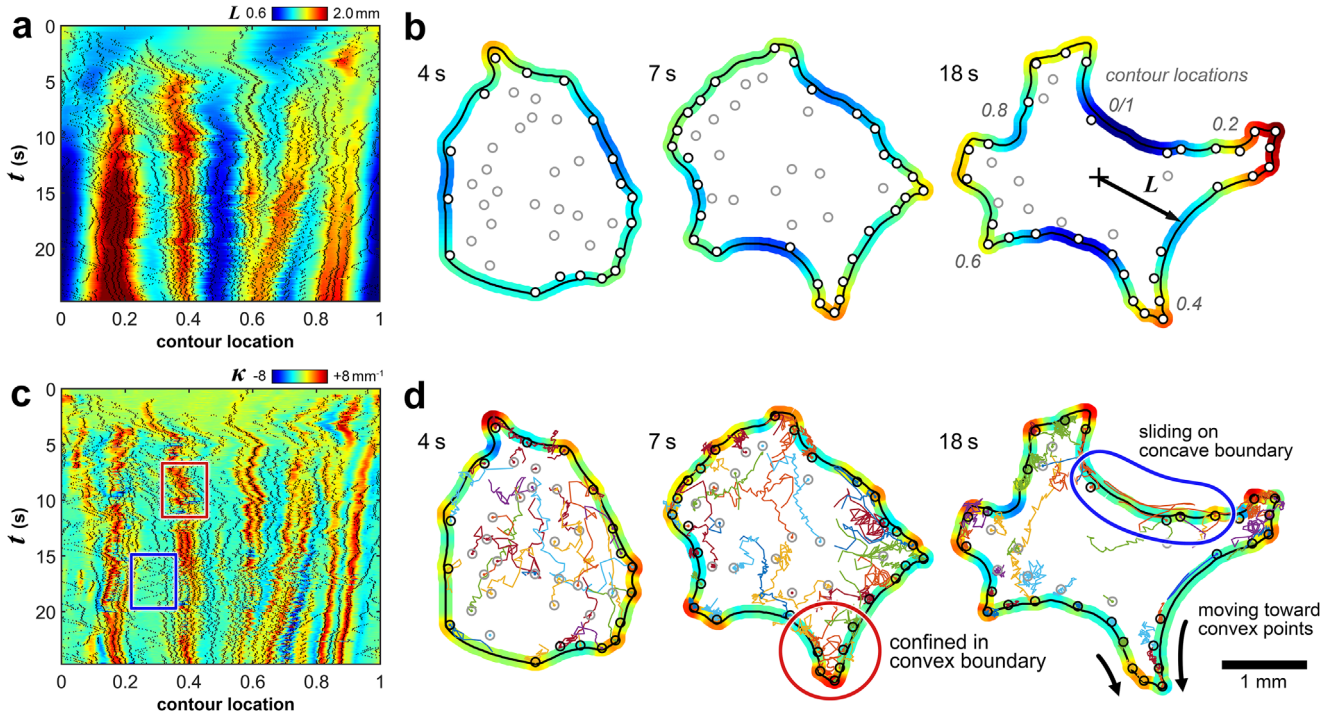

Figure 4. Shape evolution of the droplet and particle distribution on the membrane. a) Centroid-to-membrane distances, *L*, around the droplet contour at different times. Contour location is measured as a distance, normalized by the drop's perimeter length, from the drop centroid's north in a clockwise direction (starting (0) and ending (1) at the centroid's north) (see Figure 4b 18s). Particle positions on the boundary are overlayed in black dots. b) Deformation along the boundary, colored as in panel (a). c) Curvature κ (color coded) of the contour locations mapped over time, with the top of the map being time zero before the field is applied. The red square (confined particles on convex boundary) is mapped to the red circle in d), while the blue square (sliding particles on concave boundary) is mapped to the blue circle in (d). (d) Particle trajectories and distribution along the deformed boundary at evolution times of 4, 7, and 18 s.

regions of high local particle density led to three distinct deformations. The importance of low membrane surface tensions is also captured since, if it were too high, an impossible number of active particles would need to be packed along the droplet perimeter. It is worth noting that if the particles were passive Brownian spheres, their Boltzmann statistics would prohibit their accumulation at the boundary. Therefore, given the relatively low number density of particles inside the droplets, ≈27 mm^{-3}, the droplet deformations exhibited here could never be seen without particle activity.

The evolution of the droplet shape is established by active particles producing regions of high curvature, κ, on the walls of the droplet (Figure 4). Plotting the evolution of the droplet centroid-to-membrane (wall) distances for clockwise contour locations (starting (0) and ending (1) at the centroid's north, normalized by the drop perimeter length) as a function of elapsed time shows how these membrane deformations grow over time (Figure 4a). Particles start to impinge on the interface ≈2.3 s after the external field is applied, leading to the formation of membrane undulations (amplitude ≈0.05–0.2 mm). These undulations incline the membrane with respect to the rolling directions of nearby particles, and nearby particles move along the inclined membrane toward the protrusions, aggregating at regions of higher κ. This newly formed aggregate of particles collectively pushes the membrane and further amplifies undulations (amplitude ≈0.6–1.4 mm) into leading protrusion edges, with multiple smaller undulations observed to coalesce into larger, extended tendrils (Figures 4a,b, and 5a). Accordingly, small undulations of ≈0.05–0.2 mm merged into fewer but larger protrusions of ≈0.6–1.4 mm. Figure 4a,b shows the evolution of the droplet centroid-to-membrane (wall) distances as a function of elapsed time, with particles on the membrane represented as black dots. As multiple protrusion edges develop, particles at the edges continue to push the membrane at their respective locations. Figure 4b shows that narrow range of centroid-to-membrane (wall) distances of 1.2 μm (at 4 s), characteristic of a more circular shape, significantly broadens to a range from 0.56–2.24 μm (at 23 s), and the approximate locations of protrusions did not change after the initial formation of the protrusions (at 4 s).

The formation of leading protrusion edges is influenced by the initial shape of the droplet and the distribution of particles before the external field is applied. If these initial conditions could be controlled (which was difficult to achieve in our studies, given the preparation conditions we used), the nature of the shape evolution of the droplet could be manipulated. As previously discussed, droplet shape and particle motion influenced each other, leading to a configuration where multiple protrusion edges emerged from the droplet, with more particles accumulating at the leading edges. This interaction is better explained by the membrane curvature, as it defines the gradient in the slope against the rolling particles.

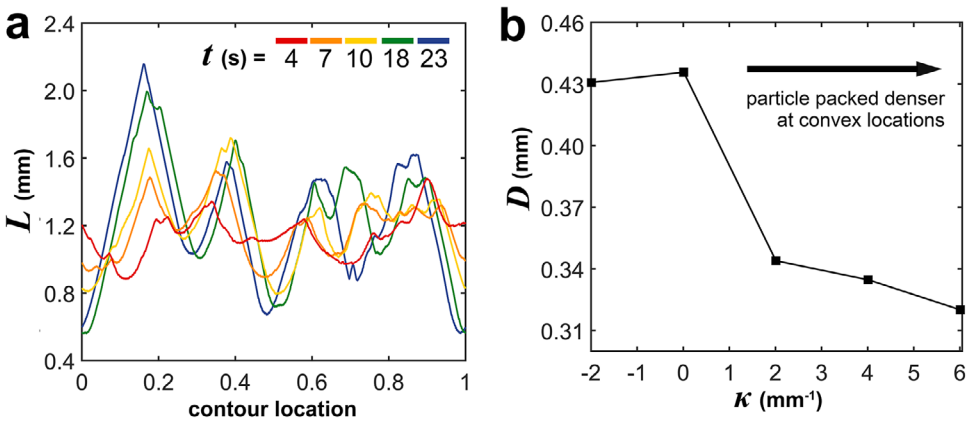

Figure 5. Shape evolution of the droplet and particle distribution on the membrane. a) Horizontal slices of the contour map in Figure 4a at different times, exhibiting growth of small undulations into fewer but larger protrusions. b) Average distances between neighboring particles, *D*, at the drop boundary after 15 s as a function of the curvature of the droplet contour.

Figure 4c,d shows the relationship between the membrane curvature and elapsed time using the same plotting procedure as in Figure 4a. The uniform positive curvature of ≈0.6 mm^{-1} increases to 8 mm^{-1} at protrusion edges. Adjacent to the edges, the membrane curves inward with a negative curvature, ranging from −1.3 to −0.6 mm^{-1}, indicating that the membrane is elongated by a point force exerted at the lead edge of the protrusion. Although the edges trap only three or less particles, neighboring particles slide toward the edge to apply additional force for the shape deformation. Figure 5b shows the average distance between two neighboring particles on the membrane as a function of the membrane curvature, at an elapsed time of 15 s. Neighboring particles are densely packed at protrusion edges that are deformed with a greater curvature. The trapped particles at the edge are exemplified by the red box/circle in Figure 4c,d. The membrane between protrusions is unstable for particles due to the negative curvature, making particles slide back and forth in this region, as depicted in the blue box/circle in Figure 4c,d.

As the protrusions grew in length, a neck formed that narrowed with extension of the protrusion to the point where separated droplets broke off when the rate of diffusion of NPs (POSS-NH_3Cl) to necking regions is much smaller than the rate of deformation during the later stage of the evolution. When the droplets split, the parent and newly formed droplets migrated in opposite directions when the force exerted on one side surpassed that on the other. In **Figure 6**a, due to the field strength being stronger near the solenoid's off-center, particles are directed along the outward field gradient once they escape the uniform field center. For protrusion edges extending to this distance, particles align horizontally along the gradient and experience stronger outward forces, leading to accelerated necking and subsequent droplet separation. When the neck breaks, liquid in the necking region occasionally traps 1–3 particles, forming a satellite droplet. Notably, with a higher membrane curvature (radius of 1.5–3*d*), the Laplace pressure $\Delta P = -2\gamma H$ (where H represents mean curvature) is approximately twice as high as that of the parent droplet when the contribution of membrane elasticity is neglected. While membrane deformations caused by the particles are rarely observed in such cases, the droplet exhibits translational and rotational motions due to the coupled movements of the particles.

To investigate the potential to generate active droplets, we changed our glass substrate to a flat silicon wafer treated by oxygen plasma to reduce adhesion between the droplets and the substrate. The biased distribution of active particles on the boundary, in which particle aggregates in regions of high curvature, induced directional motions of the droplet on the substrate. If the force applied to the membrane is greater than that between the membrane and the substrate, the entire droplet will be moved by the active particles. As shown in Figure 6b, once the active particles are confined at the leading edge of a protrusion, the deformed droplet is moved by the particle actions in the direction of protrusion growth. If the advancing contact angle of the lead edge of the protrusion is greater than the receding edge of the droplet with the substrate, the entire droplet shape will become elongated in the direction of droplet motion. If the advancing and receding contact angles are the same, the droplet will freely move without additional deformation of the droplet. This behavior also holds for droplets that break off when long protrusions or tethers narrow during growth.

Finally, we note that when the magnetic field is turned off, active particle motion and, therefore, droplet deformation immediately cease. The membrane encasing the droplet will begin to contract to reduce the interfacial area and, in so doing, will compress the NPSs at the interface, causing them to jam and lock-in the highly non-equilibrium shape indefinitely, i.e., the droplet shape has evolved. If the magnetic field is turned on again, the impingement of the active particles on the NPS membrane will break the interfacial jam of the NPSs, and the evolution of the droplet shape will resume. This cycle will continue on-demand until the supply of either the non-active NPs (POSS-NH_3Cl) or ligands is exhausted.

3. Conclusion

We demonstrate a shape-evolving system of oil droplets in water that is deformed by active magnetic rollers. The extent of the deformation of the droplets is determined by both the rollers themselves and the interfacial tension of the system, which is tuned over three orders of magnitude (from 22 down to 37 μN m^{-1}) by the adsorption of NPSs at the oil-water interface. Upon being

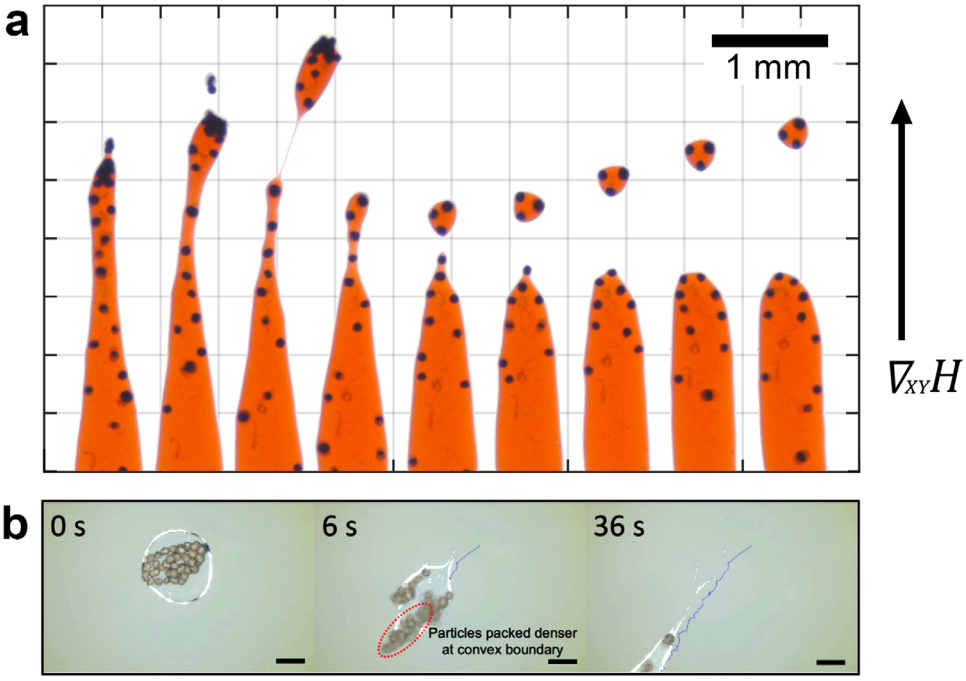

Figure 6. Directional motion of the droplets by active rollers a) The Protrusion edge creates necking and subsequent separation when it enters areas with in-plane outward field gradients. Satellite droplets showing translational and rotational motions without wall deformation. Time-lapse images from left to right at a 2 s interval. b) Particles with a biased distribution at a convex boundary location lead to droplet migration. Scale bar is 200 µm.

placed in an oscillating magnetic field, the magnetic particles begin to roll and accumulate at the edge of the droplet, leading to the formation of protrusions and liquid tendrils at sufficiently low interfacial tensions. These deformations are locked in place by the further assembly of NPSs at the newly created oil-water interface, which jam in response to thermodynamically driven reductions in interfacial area. The shape-evolving structured liquids represent a new class of materials that are biomimetic, reconfigurable, and responsive, opening pathways for autonomous synthetic machines powered by active matter.

4. Experimental Section

Preparation of Shape-Evolving Droplets: A Helmholtz coil for generating the external magnetic field was made in house, by winding an 18 gauge enameled copper wire on to a plastic spool of 13 mm height and 25 mm diameter. An Accel TS250 waveform amplifier was connected to an Agilent 33120A function generator to produce ±7.5 V peak-to-peak square waves with a maximum output current of ±6.0A to support the optimized field strength of 3.5 mT. A cell-culture dish with a 3.5 cm diameter was placed on the Helmholtz coil. The dish was fitted with a 22 mm square cover glass as a substrate.

All chemicals except for Ni particles were purchased from Sigma Aldrich. The dish was filled with a solution of poly(sodium 4-styrenesulfonate) (PSS, 70 kg mol^{-1}) in deionized water. Ni powders (−150 + 200 mesh, 99.9% trace metal basis) from Fisher Scientific were thoroughly washed by sequential bath sonication in toluene and isopropyl alcohol, followed by drying in an oven at 80 °C overnight. A stock solution of the droplet phase was prepared by dissolving POSS ([3-(2-aminoethyl)amino]propyl-heptaisobutyl substituted, 20 mg mL^{-1}) and Sudan red (1 mg mL^{-1}) in chloroform. Ni particles were sedimented in a 1.5 mL conical tube of the POSS solution, and then, using a 10 µL pipette tip, ≈3–5 µL solution with particles was deposited on the cover glass in the PSS solution. The chloroform droplet, being denser than the surrounding aqueous phase, remained stably on the substrate. Although particles dispensed through a pipette tip accumulated at a single location in the droplet, they dispersed immediately when an external field was applied.

Tracking of Droplet Shape and Particle Motions: The color movies were recorded at 19.6 fps in a 2456 × 1842 square pixel resolution by using an Olympus SZ40 stereo microscope. The entire image processing, except for single particle tracking, was conducted with MATLAB 2018b. To facilitate tracking of the droplet's evolving fronts, the droplet phase was dyed red with Sudan Red (1 mg mL^{-1}). 8-bit red color intensities in each frame were used to differentiate the droplet from the background by using the intensity thresholding, where the outermost pixels of the droplet phase were defined as the droplet membrane or wall. The level set method was used to track the membrane shape change. For every pixel in each frame, the closest distance from the droplet membrane was calculated as a level set ϕ (>0 for outside and <0 for inside the droplet). ϕ was spatially smoothed with a 2 D Gaussian blur to reduce the effects of a pixelated image. The normal vector $\vec{n}$ to the drop membrane was estimated as a spatial gradient of ϕ, i.e., $\vec{n} = \nabla\phi/|\nabla\phi|$, and the local membrane curvature was calculated from $\vec{n}$ with the equation $\kappa = \nabla \cdot \vec{n}$. The droplet deformation F between the frame intervals 0.051s was assumed to occur in $\vec{n}$ direction from the preceding frame, as expressed in $\phi_t + F|\nabla\phi| = 0$. The particle positions were determined through 2D cross-correlation of a particle and the grayscale images of blue color intensities, where the droplet was nearly invisible. The computed correlation displayed sharp peaks at particle centroids, and the positions of peak maxima were taken as particle positions in data analysis. The motions of active particles were tracked using Trackpy, a particle-tracking toolkit for Python. The local density of particles was visualized by calculating the sum of inverse distances from 10 closest particles for each pixel location.

Supporting Information

Supporting Information is available from the Wiley Online Library or from the author.

Acknowledgements

This work was supported by the U.S. Department of Energy, Office of Science, Office of Basic Energy Sciences, Materials Sciences and Engineering Division, the Molecular Foundry under Contract No. DE-AC02-05-CH11231 within the Adaptive Interfacial Assemblies Toward Structuring Liquids program (KCTR16).

Conflict of Interest

The authors declare no conflict of interest.

Data Availability Statement

The data that support the findings of this study are available from the corresponding author upon reasonable request.

Keywords

active matter, interfacial assembly, structured liquids

Received: January 17, 2025
Revised: April 19, 2025
Published online:

[1] D. L. Bodor, W. Pönisch, R. G. Endres, E. K. Paluch, *Dev. Cell* **2020**, *52*, 550.
[2] D. Holz, D. Vavylonis, *Biophys. Rev.* **2018**, *10*, 1577.
[3] M. Krause, A. Gautreau, *Nat Rev Mol Cell Bio* **2014**, *15*, 577.
[4] K. Rottner, M. Schaks, *Curr. Opin. Cell Biol.* **2019**, *56*, 53.
[5] C. Bechinger, R. Di Leonardo, H. Löwen, C. Reichhardt, G. Volpe, G. Volpe, *Rev. Mod. Phys.* **2016**, *88*, 045006.
[6] J. Weichsel, P. L. Geissler, *PLoS Comput. Biol.* **2016**, *12*, 1004982.
[7] C. Y. Jin, C. Krüger, C. C. Maass, *P Natl Acad Sci USA* **2017**, *114*, 5089.
[8] C. H. Meredith, P. G. Moerman, J. Groenewold, Y. J. Chiu, W. K. Kegel, A. van Blaaderen, L. D. Zarzar, *Nat. Chem.* **2020**, *12*, 1136.
[9] S. Birrer, S. I. Cheon, L. D. Zarzar, *Curr Opin Colloid In* **2022**, *61*, 101623.
[10] C. Xu, N. Martin, M. Li, S. Mann, *Nature* **2022**, *609*, 1029.
[11] T. Sanchez, D. T. N. Chen, S. J. DeCamp, M. Heymann, Z. Dogic, *Nature* **2012**, *491*, 431.
[12] R. Adkins, I. Kolvin, Z. H. You, S. Witthaus, M. C. Marchetti, Z. Dogic, *Science* **2022**, *377*, 768.
[13] A. M. Tayar, F. Caballero, T. Anderberg, O. A. Saleh, M. C. Marchetti, Z. Dogic, *Nat. Mater.* **2023**, *22*, 1401.
[14] T. Gao, Z. R. Li, *Phys. Rev. Lett.* **2017**, *119*, 108002.
[15] L. J. Ruske, J. M. Yeomans, *Phys. Rev. X.* **2021**, *11*, 021001.
[16] Y. X. Gao, Y. Guo, Y. R. Yang, Y. P. Tang, B. Wang, Q. H. Yan, X. Y. Chen, J. X. Cai, L. Fang, Z. Xiong, F. Gao, C. J. Wu, J. Z. Wang, J. Y. Tang, L. Shi, D. Li, *Adv. Mater.* **2024**, *36*, 2305632.
[17] G. Kokot, H. A. Faizi, G. E. Pradillo, A. Snezhko, P. M. Vlahovska, *Commun Phys-Uk* **2022**, *5*, 91.
[18] L. Fang, X. Y. Liu, Y. X. Gao, Y. Y. Lin, K. Wu, J. Z. Wang, W. G. Lu, D. Li, *Sci. China Mater.* **2024**, *67*, 179.
[19] S. C. Takatori, A. Sahu, *Phys. Rev. Lett.* **2020**, *124*, 158102.
[20] H. R. Vutukuri, M. Hoore, C. Abaurrea-Velasco, L. van Buren, A. Dutto, T. Auth, D. A. Fedosov, G. Gompper, J. Vermant, *Nature* **2020**, *586*, 52.
[21] J. Diaz, I. Pagonabarraga, *Mol. Phys.* **2024**, *122*, 2378117.
[22] J. Forth, P. Y. Kim, G. H. Xie, X. B. Liu, B. A. Helms, T. P. Russell, *Adv. Mater.* **2019**, *31*, 1806370.
[23] A. Kaiser, A. Snezhko, I. S. Aranson, *Sci. Adv.* **2017**, *3*, 1601469.
[24] B. A. Grzybowski, H. A. Stone, G. M. Whitesides, *Nature* **2000**, *405*, 1033.
[25] X. B. Liu, N. Kent, A. Ceballos, R. Streubel, Y. F. Jiang, Y. Chai, P. Y. Kim, J. Forth, F. Hellman, S. W. Shi, D. Wang, B. A. Helms, P. D. Ashby, P. Fischer, T. P. Russell, *Science* **2019**, *365*, 264.
[26] W. Yan, J. F. Brady, *Journal of Fluid Mechanics* **2015**, *785*, R1.
[27] W. Yan, J. F. Brady, *Soft Matter* **2018**, *14*, 279.
[28] I. Berdakin, Y. Jeyaram, V. V. Moshchalkov, L. Venken, S. Dierckx, S. J. Vanderleyden, A. V. Silhanek, C. A. Condat, V. I. Marconi, *Phys. Rev. E.* **2013**, *87*, 052702.
[29] X. B. Yang, M. L. Manning, M. C. Marchetti, *Soft Matter* **2014**, *10*, 6477.